Surface wave quantification in a highly heterogeneous alluvial basin: Case study of the Fosso di Vallerano valley, Rome, Italy

Kristel Carolina Meza Fajardo, Chiara Varone, Luca Lenti, Salvatore Martino, Jean François Semblat

Surface wave quantification in a highly heterogeneous alluvial basin: Case study of the Fosso di Vallerano valley, Rome, Italy

By

Kristel C. Meza-Fajardo [(1)*], Chiara Varone [(2)], Luca Lenti[(3)], Salvatore Martino[(4)], Jean-François Semblat[(5)]

Submitted to:

Soil Dynamics and Earthquake Engineering

AUTHORS' AFFILIATIONS:

(1) Seismic and Volcanic Risk Unit, Risk and Prevention Division, BRGM.

(2) École Supérieure d'Ingénieurs des Travaux de la Construction de Paris (ESITC Paris).

(3) Department GERS. University Paris-Est / The French institute of science and technology for transport, development and networks (IFSTTAR).

(4) Department of Earth Sciences and Research Center for Geological Risks (CERI) of the University of Rome "Sapienza".

(5) École Nationale Supérieure de Techniques Avancées (ENSTA) ParisTech, IMSIA UMR 9219.

* **Corresponding author:**

Seismic and Volcanic Risk Unit, Risk and Prevention Division, BRGM.

3, avenue Claude-Guillemin, BP 36009 - 45060 Orléans cedex 2 – FRANCE

Tel : +33 (0) 2 38 64 36 91

E-mail : k.mezafajardo@brgm.fr

ABSTRACT

The Vallerano district in Rome is built on an alluvial valley with a very complex geological setting (highly heterogeneous soil deposits) due to the depositional activity of Tiber River tributaries ongoing since the Pleistocene age. A high-resolution engineering-geological model of the valley was reconstructed through field investigations, boreholes log-stratigraphies and geophysical investigations. 2D FEM numerical modelling of the alluvial valley allowed to assess the local response in terms of seismic wave propagation on surface, amplification function and cumulative kinetic energy. Soil layering and basin effects combine to induce a complex local seismic response. Different typologies of seismic waves are present in the seismograms and surface waves have been also detected. Retrograde Rayleigh surface waves have been identified and extracted through a procedure based on the time-frequency normalized inner product. The spatial analysis of the extracted Rayleigh waves highlights that the local seismic response of the valley is strongly influenced by edge-generated surface waves. The results suggest that amplification is strongly related to the thickness of the soil deposits, whereas the elongated duration is more related to a layered basin structure. The soil layering and the basin effects on the generation of surface waves have been assessed and quantified.

Keywords: *basin effects, site characterization, surface waves*.

1. Introduction

Seismograms observed at sedimentary basins are usually characterized by late-arrivals of long-period phases. Precise knowledge of the characteristics of such long-period ground motions generated in basins is now considered a crucial element in the modern design of large scale structures. Recent events around the world have illustrated the unordinary damage to large-scale structures caused by long-period ground motions, being distinctive examples the 1985 Michoacan earthquake in Mexico (e.g,. [1]), and the 2012 Emilia earthquake in Northern Italy [2]. It is well recognized that the long-period motions are mainly composed of surface waves, generated by conversion of body wave energy as it propagates through sedimentary basins. Several researchers have observed that surface waves are induced at basin edges due to the incidence of S-waves of shallow and regional earthquakes (e.g., [3–5]). Many observational studies have investigated the characteristics of the so called "basin-induced surface waves" (such as duration and central frequency) and found a strong dependence on the basin heterogeneity (*e.g.*, [6,7]). A wave propagation analysis based on a heterogeneous basin model is thus necessary to characterize strong ground motion in sedimentary basins.

With the advances in numerical techniques and computational power, it is now possible to estimate the amplitude of the seismic phases propagating in a realistic model of a heterogeneous basin. Accurate simulations have been performed for Los Angeles basin in the United States with the Finite Difference Method [8], the Kanto basin in Japan with Gaussian Beam Method [9], and the Mygdonian basin in Greece with the Spectral Element Method [10]. Furthermore, several techniques to characterize ground motion have been proposed in the past in the context of site effects estimation, such as the Standard Spectral Ratio [11], the Horizontal-to-Vertical (H/V) Fourier Spectral Ratio [12], and the Group-Delay Spectrum [13]. Whereas most classical signal processing studies are aimed at quantifying frequency-dependent characteristics of the ground motion at a site, it is now well recognized that many signal processing problems can be advantageously phrased in a time–frequency language, in particular in the case of non-stationary signals for which the frequency content varies with time. Recently [14] developed a technique to identify and extract surface waves from one-station, three-component seismograms. This time-frequency technique allows one to identify the Rayleigh waves that are present in the signal, as well as to differentiate between prograde and retrograde particle motion. The technique is equally effective in identifying and extracting Love waves [15]. The procedure, referred to as the 'Normalized Inner Product' (NIP), is based on the Stockwell Transform [16] and has been applied to successfully identify surface waves from seismograms recorded on sedimentary basins in Japan, the United States, Taiwan and New Zealand [14,15].

In the present study, we use the NIP to study surface wave propagation and basin effects from numerical simulations on the Fosso di Vallerano valley in the southern district of Rome, Italy. The ground motion time-histories were generated with the Finite Element Method in the time domain (CESAR-LCPC code, [17]), for a previous study on the influence of the buildings presence on the spatial variability of ground motion on this valley [18]. Because two 2-D numerical models of the basin were constructed to describe the heterogeneity of the basin along two directions (profiles), we focus our attention on Rayleigh wave propagation in this study. First, a brief review of the geological setting of the Fosso di Vallerano valley is given along with the procedure to construct the basin model. Second, details of the FEM simulations are provided and some wave propagation maps are presented for the two profiles. Finally, waveforms and spectrograms of the identified and extracted Rayleigh waves are presented and used to investigate the influence of the heterogeneity of the basins.

2. The Fosso di Vallerano Valley

2.1 Location

The Fosso di Vallerano is an alluvial valley in the southern district of Rome's urban area, approximately at 10 km SE from the historical center of the city. It is located within the XII sub-municipality of Rome as shown in Figure 1a. The Fosso di Vallerano valley was selected for this study because of its complex geological setting (highly heterogeneous soil deposits) and because of the important urban expansion recently taking place in the surrounding area. Most of the anthropogenic structures in the area are residential buildings with reinforced concrete bearing structure and height varying between 15 and 120 m. The valley is part of the drainage basin of the left tributary of the Tiber River, which extends from SE to NW and drains surface water from the Alban Hills and Castel Gandolfo area to the Tiber River [19]. This basin consists of two sub-basins that join before the Tiber River's confluence: the Vallerano creek in the SE portion and the Cecchignola creek in the NE portion. The complex geomorphological setting of the area is due to a series of successive deviations and rearrangements of the riverbed during the Würmian glacio-eustatic cycle [20]. In this study we focus on a flat portion of the Fosso di Vallerano valley (shown in Figure 1b), limiting to the north with the Montorio hill, to the east with the Monte delle Pozzonale hill, to the west with the Torrino hill, and partially with the Castellaccio hill to the south.

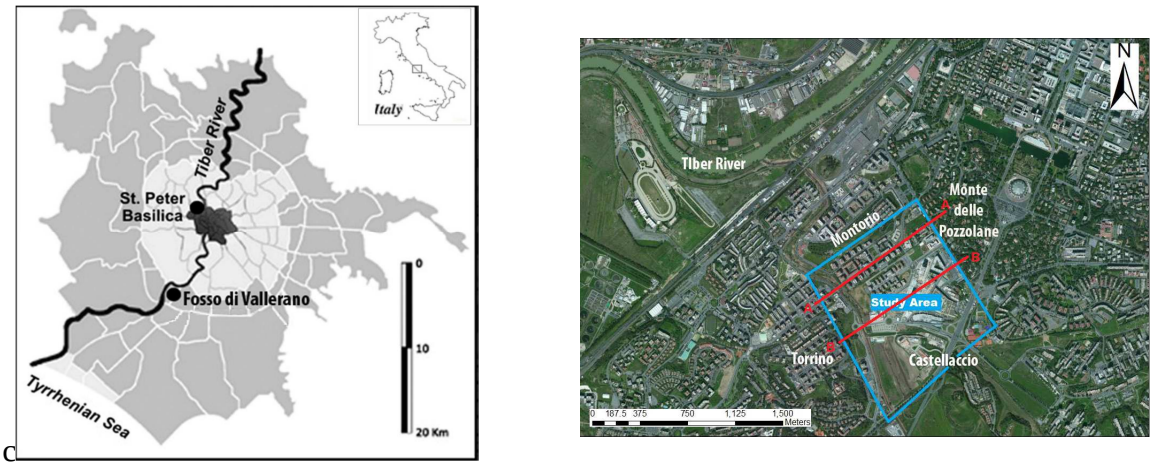

Figure 1. Location of study area. a) Location of the Fosso di Vallerano valley within the municipality of Rome. b) Satellite view of the Fosso di Vallerano area. The blue line borders the portion of Fosso di Vallerano valley in which this study is focused on. The red lines correspond to two profiles used for analysis of basin effects.

2.1 Geological setting and characterization

The geological evolution of Rome can be related to three different processes: (i) a combination of Miocene to Early Pleistocene extensional tectonic phases related to the Apennines' back-arc evolution [21], (ii) a Middle-Late Pleistocene phase in close connection with sea level oscillations [22], and (iii) the activity of the volcanic district that surrounds the city [23]. Whereas the different sedimentary deposits in the Rome area can be associated to marine sedimentary cycles from many marine transgressions [24], the volcanic activity around Rome led to continuous deposition of pyroclastic deposits in the fluvial valley. Within such geological setting, it can be argued that the Tiber River and its tributary valleys are composed of

heterogeneous soft alluvial deposits while relieved areas are mainly composed by stiff volcanic deposits.

A high-resolution engineering geological model of the Fosso di Vallerano valley has been developed through several geotechnical investigations and geophysical measurements (seismic noise recordings) [25]. Available log-stratigraphies from 250 boreholes are available [19] as well as one cross-hole test and expeditious geomechanical on-site investigations (Pocket-Penetrometer and Pocket Vane-test) [19,26]. Five main litho-stratigraphic groups were distinguished based on the collected data [25]:

1) Plio-Pleistocene marine sediments (PP) which represent the geological bedrock of the area;
2) Pleistocene alluvial sediments (PT) that were deposited by the Paleo-Tiber 4 River [27];
3) Volcanic deposits (VL) that erupted from the Alban Hills and the Monti Sabatini volcanic district [28];
4) Pre–Würmian fluvio-palustrine deposits (FP) [29];
5) Recent alluvial deposits (AL) that filled the valley incisions since the end of the Würmian regression to the present [30];

The cross sections shown in Figure 2 depict a complex geological and geomorphological setting of the valley. Their location in the study area is indicated by the red lines in Figure 1b. Cross section AA' is characterized by the presence of a single-shape alluvial valley, whereas cross section BB' is characterized by a double-shape alluvial valley (i.e. two different fluvial engraves are included in the same valley). Such a peculiar geological setting can be related to syn-sedimentary tectonic activity that dislocated the geological bedrock (PP units) and the overlying PT deposits, leading to a horst and graben structure [25]. The structural setting and the marked horizontal and vertical heterogeneities can be regarded as preparatory factors to seismic site effects in this area of Rome [31].

2.2 Finite Element model

The analysis of dynamic properties of the soil layers of the Fosso di Vallerano valley was performed at a single location and then the obtained stratigraphy was extrapolated to the area taking into account the reconstructed high-resolution geological model. Velocity profiles were derived using numerical simulations of wave amplification in 1-D soil columns and comparing them with spectral ratios (SR) of recorded events. Each numerical simulation was performed by applying separately the horizontal components (NS and WE) of each recorded earthquake. An average function with its standard deviation was then computed to be compared to the average SR, which represents the experimental amplification function. A "trial and error" convergence was adopted to best fit the experimental amplification function with the numerical function. The resulting shear velocity values obtained in this manner for the soil layers shown in Figure 2 and which were retained for the numerical model are listed in Table 1. A more detailed description on how the shear velocity for the layers was estimated can be found in [25].

2D Numerical models along the cross sections AA' and BB' were constructed based on the engineering-geological properties of the subsoil. The geometry of the cross sections is shown in Figure 3 and all mechanical properties adopted for the different soil layers are listed in Table 1, where ρ is the soil density, Vs and Vp are the S and P wave velocity respectively, ν is the Poisson ratio, and G and E are the shear and Young's modulus respectively. Typical damping

ratios ξ were adopted for the soil layers to model energy dissipation characteristics. The bedrock below the alluvial deposits is modeled as a half space, truncated with absorbing boundaries. The input motion was applied along the entire line indicated by the arrows, therefore it was identical and uniformly distributed within the seismic bedrock as illustrated in Figure 3.

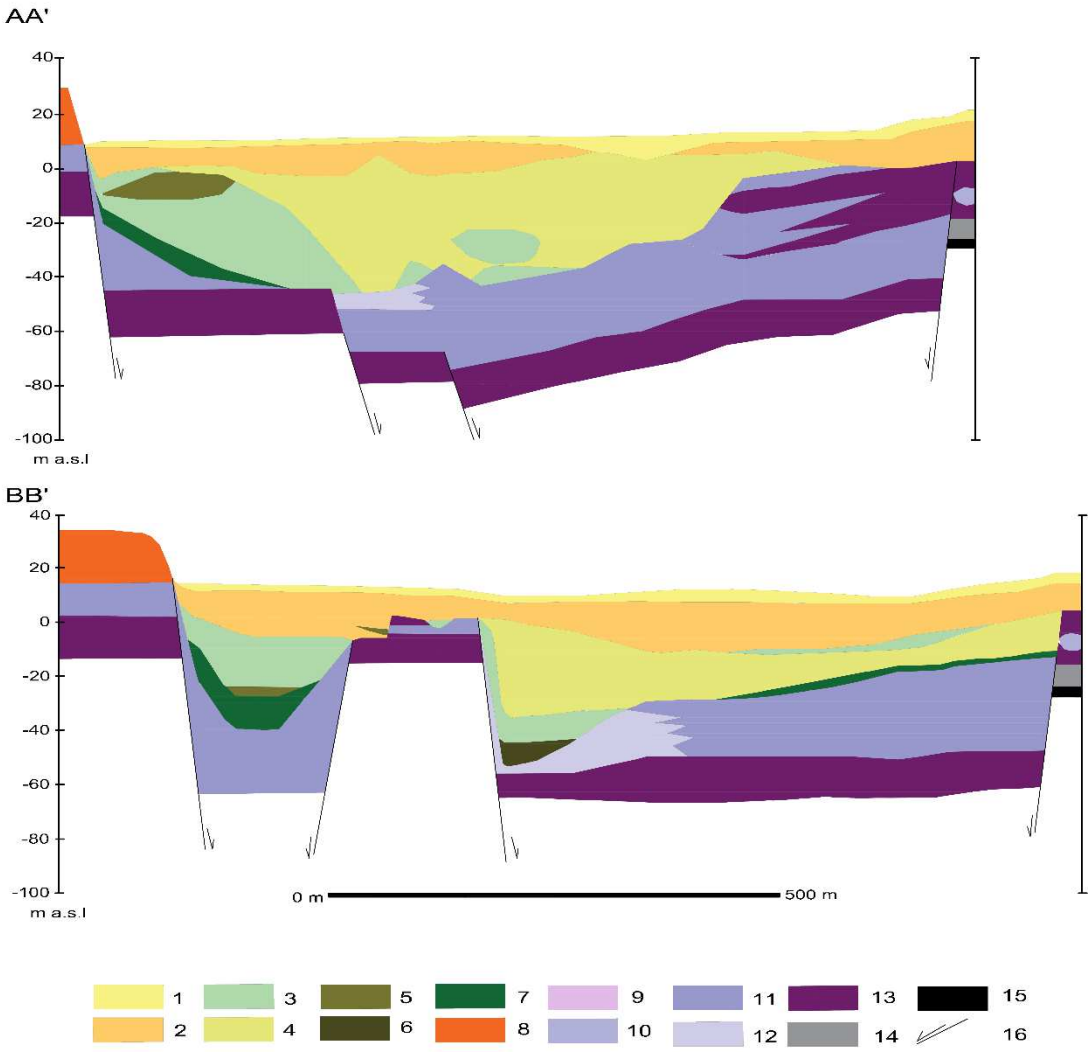

Figure 2. Geological structure of cross sections AA' and BB'. Modified from [25] . 1) Anthropic filling material; 2) Sandy-Clays characterized by a marked volcanic component; 3) Peaty clays, plastic; 4) Clays and silts, plastic; 5) Peat; 6) Sands and silty sands; 7) Polygenic, loose and heterometric gravels, with volcanic and sedimentary components. 8) Undifferentiated pyroclastic material; 9) Fluvio-palustrine deposits composed of loose gravels, sands and silts; 10) Sandy clays and silts, sometimes with freshwater gastropods; 11) Clays and silts with peaty layers; 12) Sands and silty sands; 13) Loose gravels with heterometric sedimentary component; 1) Marine clays and silty clays; 15) Marine sands and silty sands; 16) Fault; 17) Borehole.

The 2D numerical simulations were carried out with the Finite Element Method (with the code CESAR-LCPC, a code dedicated to civil, tunnel and geotechnical engineering [17]). The two cross

sections AA' and BB' were discretized using three-noded linear elements with element size limited by the minimum propagating wavelength λ to avoid significant numerical dispersion. A suitable element size Δh is the defined with the following relationship [32]:

$$\Delta h = \frac{\lambda}{12} \tag{1}$$

Table 1. Mechanical properties attributed to the various materials in the numerical geological models. Modified from [25].

Lithological units	ρ (kg/m^3)	Vs (m/s)	Vp (m/s)	ν	G (MPa)	E (MPa)	ξ (%) Strain:0.001%
1	1732.9	118	221.3	0.30	24.3	60.6	1
2	1682.0	225	420.9	0.30	85.1	212.9	1
3	1753.3	150	280.6	0.30	39.4	98.6	3
4	1865.4	235	439.6	0.30	103.0	257.5	2
5	1294.6	140	261.9	0.30	25.4	63.4	1
6, 12	1957.2	417	780.1	0.30	340.3	850.8	1
7	2140.7	713	1333.9	0.30	1088.3	2720.6	1
8	1834.9	1100	1905.3	0.25	2220.2	5550.5	1
9	2140.7	550	1028.9	0.30	647.6	1618.9	1
11	1865.4	357	667.9	0.30	237.7	594.4	3
10	1865.4	250	467.7	0.30	116.6	291.48	3
13	2140.7	1100	2057.9	0.30	2590.2	6475.5	1
Bedrock	2140.7	1100	1905.3	0.25	2590.2	6475.5	0.5

Element sizes of 1 m for the alluvial filling and of 10 m for seismic bedrock were chosen for both cross sections in order to make simulations with a maximum frequency of 10 Hz according to the lowest S-wave velocity of the alluvial deposits (118 m/s) and the largest S-wave velocity (1100 m/s) for the seismic bedrock. A set of heterogeneous absorbing layers based on Rayleigh/Caughey damping formulation [33] is placed at the lateral and bottom boundaries of the models to avoid spurious waves that may be reflected at the truncation boundaries of the numerical model. This system consists of 5 sub-layers with a damping value ξ = 0.10 in the inner portion of the absorbing layer, increasing gradually to 1.00 (at the extreme boundary of the absorbing layer).

3. Numerical simulations of wave propagation

The cross sections are subjected to seismic excitation in the form of vertically incident plane S waves. Because we are interested in the analysis of Rayleigh waves, we set a peak unitary vertical displacement. The time variation of the input motion is given by a 0th-order Ricker wavelet with frequency content from 0.1 to 15 Hz. To investigate the effects of the valley on the wave field, several recording stations (receivers) are selected along the free surface of the cross sections, as shown in Figure 3.

The results of the simulations for the two cross sections are shown in Figure 4 and Figure 5, where displacement histories at the receivers are displayed. Visual inspection of the figures show a later arrival time of the first phases at the center of the basins, a consequence of the lower velocity of propagation in the soft layers. We can also observe how low frequency phases are more distributed in time for the stations at the center of the basins, signaling dispersion as one

basin effect. In station 31 of cross section BB' however, the later phases present in the time history appear of higher frequency, which is more related to the interaction of the waves generated at the two basins than to dispersive phenomena. A more detailed account of basin effects is presented in the following section, where a time-frequency processing is applied to the time histories.

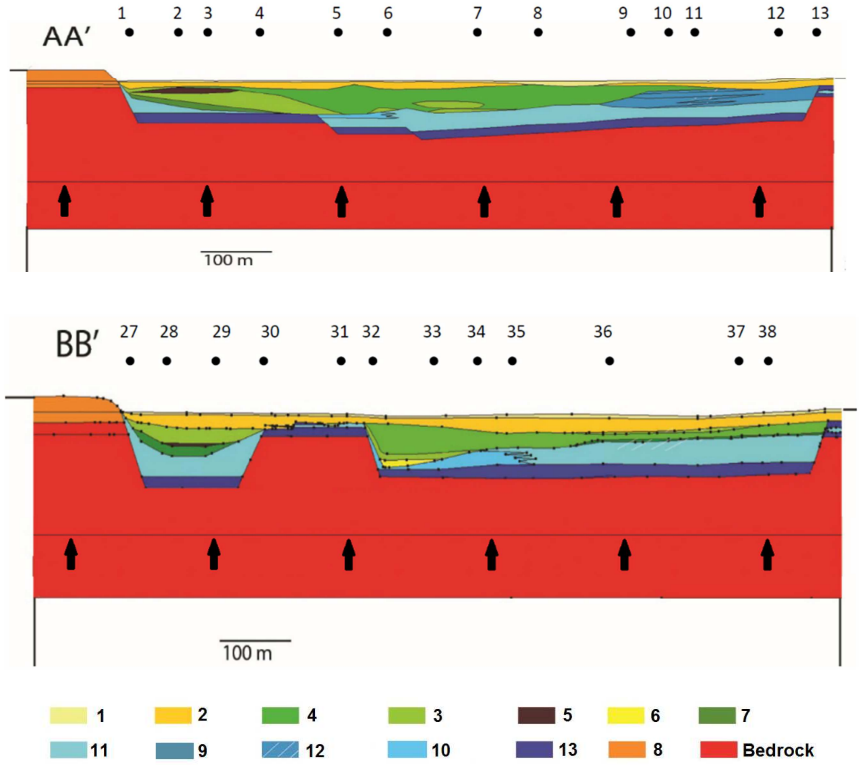

Figure 3. Numerical models for cross sections AA' and BB'. The position of the seismic inputs is also indicated. The numbered black circles indicate the location of the receivers.

(a) (b)

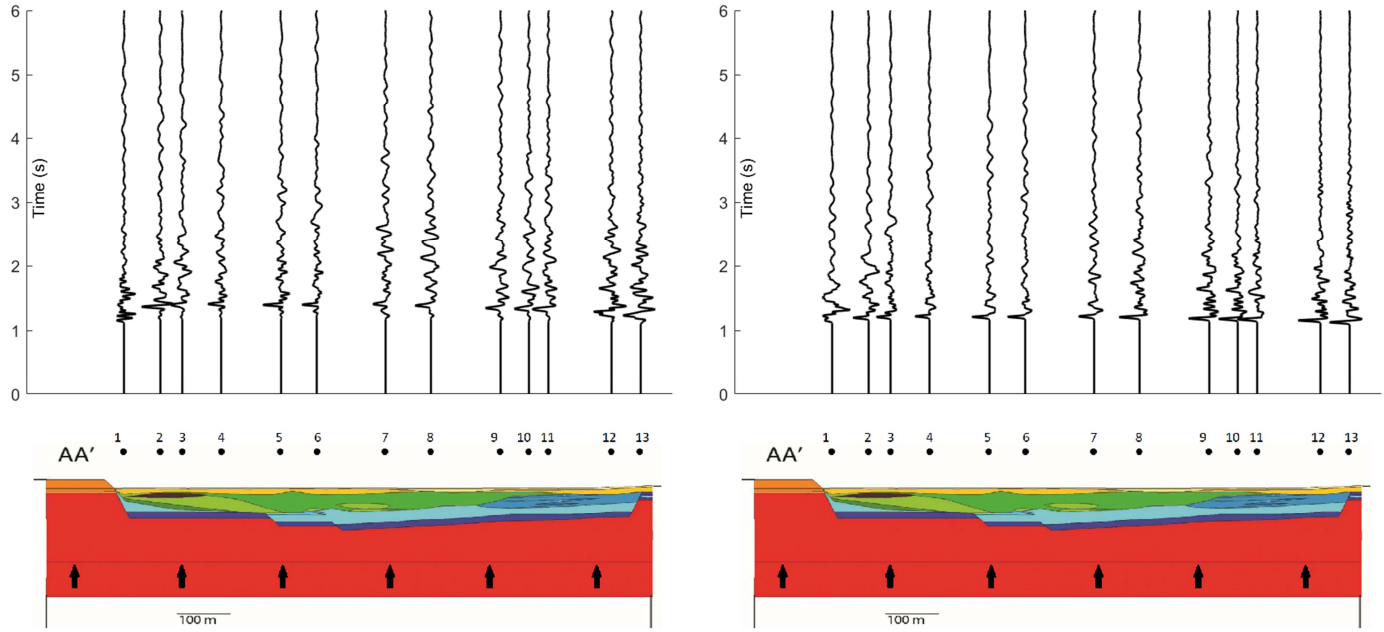

Figure 4. Displacement histories for receivers at the free surface of cross sections AA'. (a) Horizontal component, (b) Vertical component.

205

206

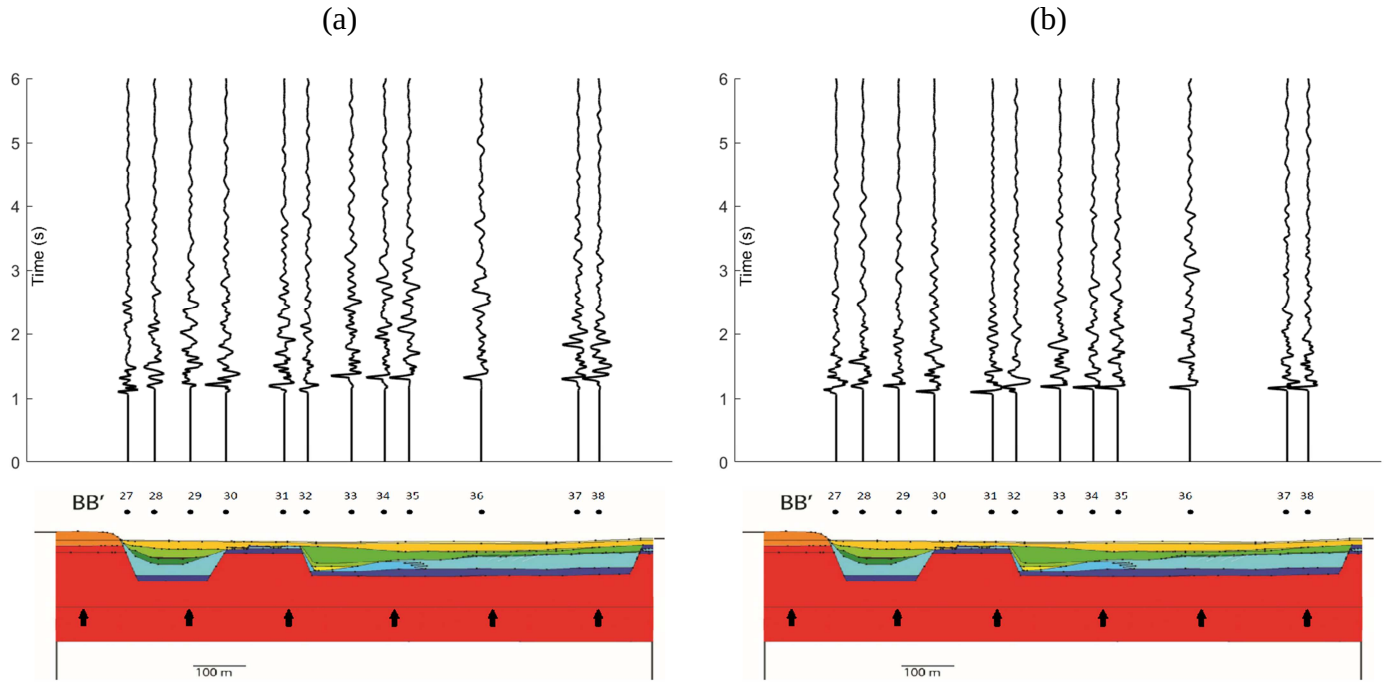

Figure 5. Displacement histories for receivers at the free surface of cross sections BB'. (a) Horizontal component, (b) Vertical component.

4. Extraction of Rayleigh waves from simulated ground motions

In this section we use the time-frequency method based on the Normalized Inner Product (NIP) to identify and extract the surface waves generated by the complex structure of the basin [14]. The basic idea of the method is to separate the waves by using the representation of their polarization characteristics in a time□frequency correlation. Each component of the seismogram is first resolved in the time-frequency domain by using the Stockwell Transform [16] :

$$S(t,f) = \int_{-\infty}^{\infty} h(\tau)\frac{|f|}{\sqrt{2\pi}}\exp\left[-\frac{(t-\tau)^2 f^2}{2}\right]\exp(-2\pi i f\tau)d\tau \tag{2}$$

We denote the Stockwell transforms of the horizontal and vertical components of the signal by $S_H(t,f)$ and $S_V(t,f)$, respectively. Each of these discrete Stockwell transforms is a matrix defined in the discretized (t,f) space, and each element of the matrix is a complex number. Therefore, each Stockwell Transform may be expressed as follows:

$$\begin{aligned} S_c(t,f) &= \mathrm{Re}\{S_c(t,f)\} + i\cdot \mathrm{Im}\{S_c(t,f)\} \\ &= A_c(t,f)\exp[i\cdot\Phi_c(t,f)] \end{aligned} \tag{3}$$

Where $i=\sqrt{-1}$, $A_c(t,f)$ is the amplitude of $S_c(t,f)$, and $\Phi_c(t,f)$ is its phase. Then, the time□frequency seismograms are filtered using the "normalized inner product" (NIP) which is a surrogate of the time-domain "correlation":

$$NIP(S_H, S_V) = \frac{\mathrm{Re}\{S_H(t,f)\}\mathrm{Re}\{S_V(t,f)\} + \mathrm{Im}\{S_H(t,f)\}\mathrm{Im}\{S_V(t,f)\}}{A_H(t,f)A_V(t,f)} \tag{4}$$

The inner product is a simple, well-known, mathematical relation used to identify orthogonality properties between two entities. It turns out to be useful to identify Rayleigh waves since there is a ±(π/2) phase shift between its horizontal and vertical components. Furthermore, if we perform a ±(π/2) shift in the vertical component S_V of the Rayleigh wave, then the resulting Transform $\hat{S}_V$ will be in phase with the horizontal component and $NIP(S_H, \hat{S}_V) = 1$. Then, using the relation $NIP(S_H, \hat{S}_V)$ we can construct simple filters to retain only those regions in the time-frequency space in which the value of $NIP(S_H, \hat{S}_V)$ is close to 1 [say, $NIP(S_H, \hat{S}_V) \geq 0.8$] and setting the rest of the time-frequency space equal to zero. Finally, the time-domain horizontal and vertical components of the Rayleigh wave are obtained directly by inverting the filtered Transforms.

To illustrate the procedure, in Figure 6 we show the Stockwell Transforms of the horizontal and vertical components at station 13. We can observe that in the vertical component most of the energy is concentrated before 2 seconds, whereas in the horizontal component dominant frequencies are more distributed in time. In Figure 7a we show the relation $NIP(S_H, \hat{S}_V)$, and we clearly observe the red regions that indicate $NIP(S_H, \hat{S}_V) \sim 1$. We then construct a filter, which is a simple time-frequency function that exclude (with zero values) the regions that are not dark red, as to isolate the Rayleigh waves. Figure 7b and 7c illustrate the filters constructed in this manner for station 13, when applied to the Stockwell Transforms of the horizontal and vertical components, respectively. The filters exclude the black regions shown in Figure 7b and 7c. We can observe that even though low frequencies are present in the seismogram at station 13, most of the energy in the form of Rayleigh waves is within 5 and 10 Hz. Finally, after applying the filter to the two components, we use the inverse Stockwell Transform to obtain the time histories of the extracted Rayleigh waves, which are shown in Figure 8. The vertical component has a –π/2 shift to show that the extracted waves have the polarization characteristics of Rayleigh waves. We can observe that the Rayleigh wave induced by the basin edge at station 13 has horizontal and vertical components with similar amplitudes.

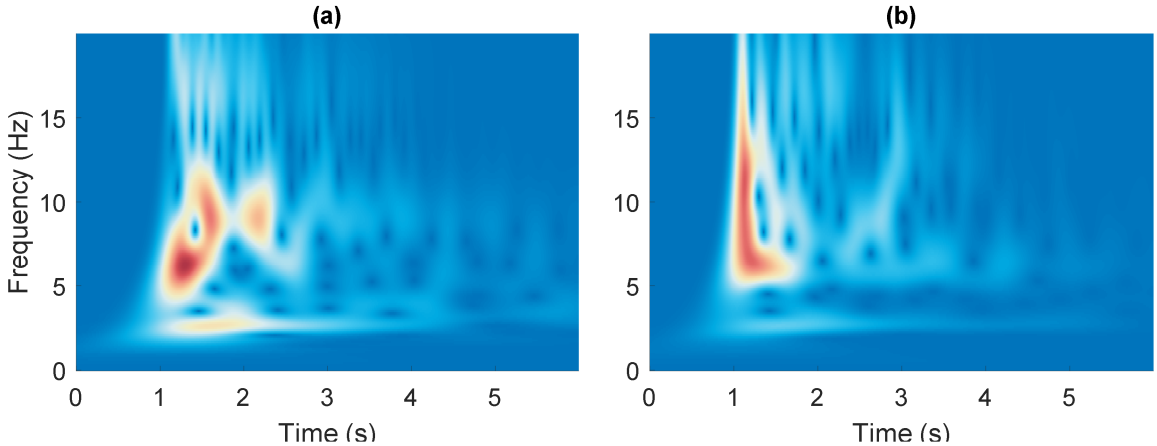

Figure 6. Stockwell Transforms of displacement components at station 13 of cross section AA'. (a) Horizontal component, (b) Vertical component.

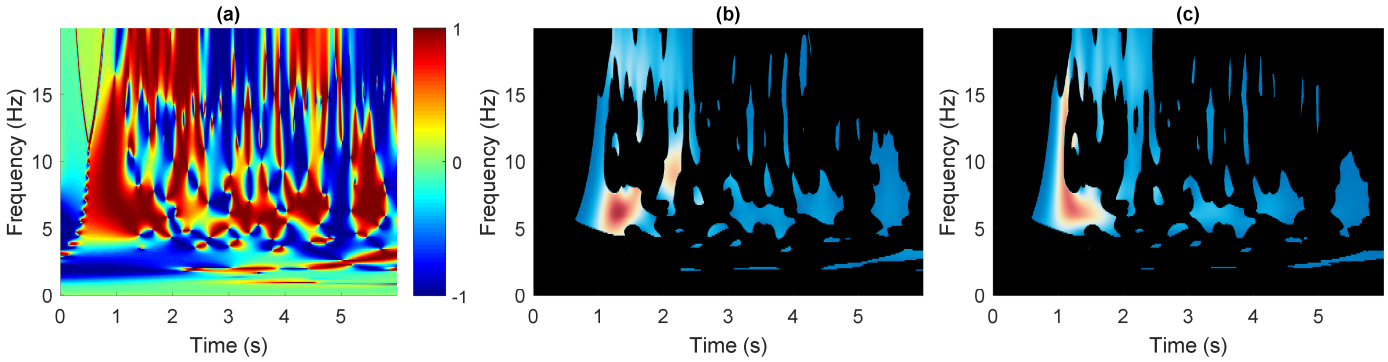

Figure 7. Isolation of Rayleigh waves through filtering of Stockwell Transforms of displacement components at station 13. (a) $NIP(S_H, \hat{S}_V)$, (b) Filter applied to Transform of horizontal component, (c) Filter applied to Transform of vertical component.

246

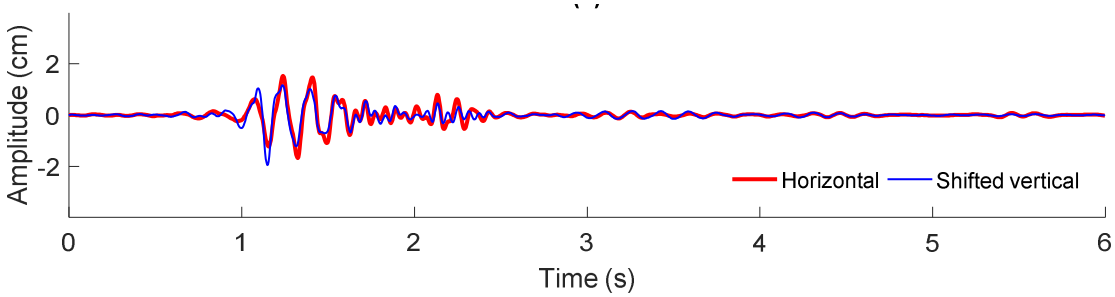

Figure 8. Horizontal and vertical components of extracted Rayleigh waves at station 13. The vertical component has a -π/2 shift.

247

248 Similar time histories of the two components of the extracted Rayleigh waves are shown in
249 Figure 9, for all the other stations in cross sections AA' and BB'. We can observe on both cross
250 sections that the Rayleigh waves with higher amplitudes are found in those stations close to the
251 basin edges. Even at station 32, there is a strong Rayleigh wave due to the presence of a close
252 (even internal) edge, so from this point of view we could consider section BB' as composed of
253 two basins. However, the edge-generated Rayleigh waves do not seem to preserve their
254 amplitude in the more internal stations of the basins, probably due to inelastic attenuation and the
255 interference of all waves diffracted by the complex soil layering. At station 8 of section AA' we
256 can observe the presence of a Rayleigh wave with high amplitude and long duration, of lower
257 frequency. The concentration of energy giving rise to this wave might be possible due to the very
258 thick soil deposits (layers 4 and 11) below the station. A similar structure of the soil deposits is
259 not present in section BB' and the Rayleigh waves we identified are weaker, even at station 33
260 under which there is a thick soft layer (layer 4). On the other hand, we could claim that there are
261 no extracted surface waves at stations 6 and 29 as there are no clear extracted wavetrains, and
262 that the motion shown in Figure 9 at those stations is simply numerical noise.

263

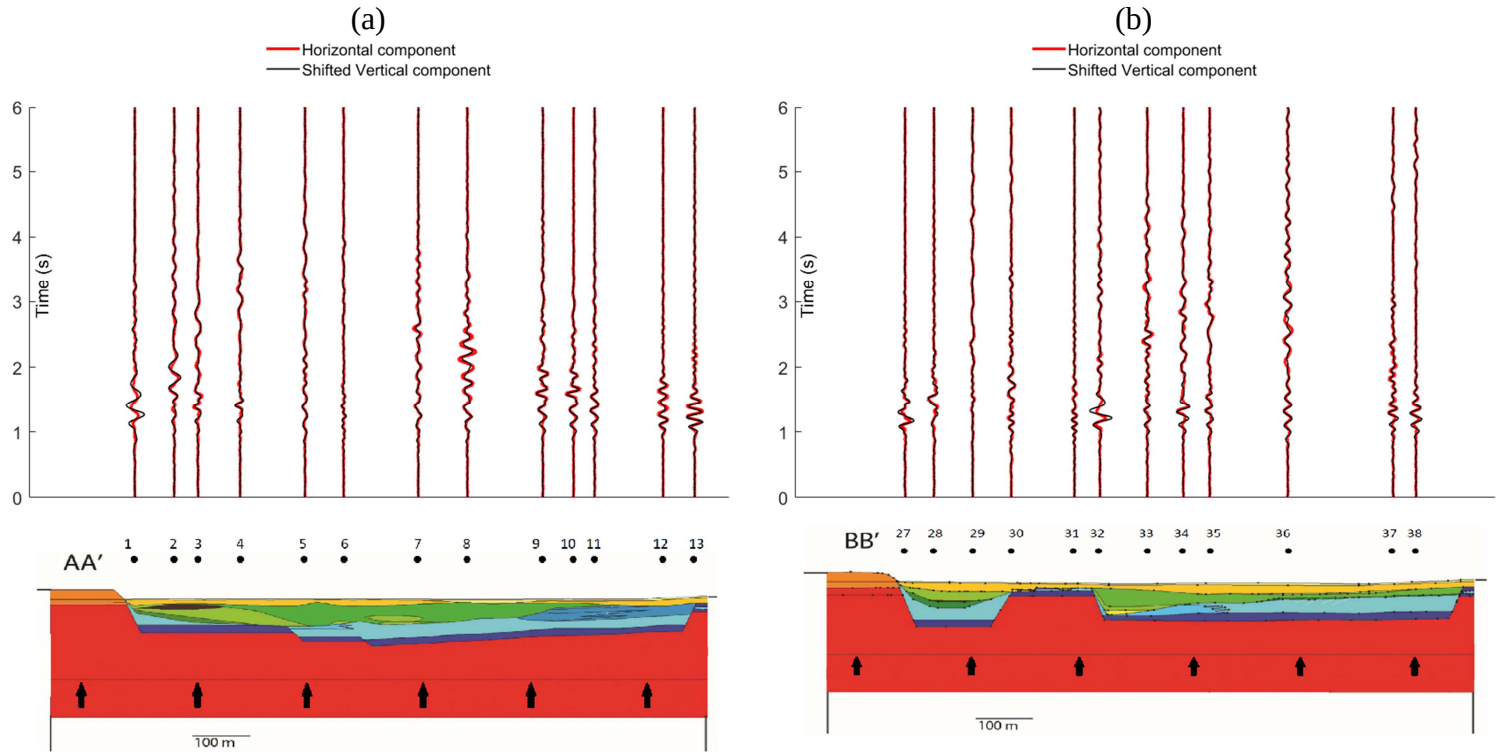

Figure 9. Horizontal and vertical components of extracted Rayleigh waves at stations on cross sections AA' and BB'. (a) Stations on profile AA', (b) Stations on profile BB'. The vertical component has a -π/2 shift.

The evolution of the frequency content of the extracted waves can be appreciated from Figure 10, where we present the Stockwell transforms of the vertical component. On the top of the figures we have plotted (the black circles) the predominant frequency (the frequency of maximum amplitude of the Transform) at each station. In the same plot we show at each station the energy ratio, that is, the ratio of the total energy of the extracted waves and the total energy of the entire seismogram. We define such ratio with the following expression:

$$Energy\ ratio = \frac{\iint \left|S_{V\_extracted}(t,f)\right|^2\ dt\ df}{\iint |S_V(t,f)|^2\ dt\ df} \quad (5)$$

where $S_{V\_extracted}(t,f)$ denotes the Stockwell transform of the extracted Rayleigh waves. We observe that the extracted Rayleigh waves are an important fraction of the total energy in the seismograms, with the highest values at the edges of the basins, where they are generated. Furthermore, the Rayleigh waves generated at the eastern (right) edge of both cross sections are of higher frequency (> 5 Hz) when compared to other stations, associated to the predominance of stiffer soil layers (layers 11 and 10) at those eastern edges. We can also observe that the predominant frequency of the Rayleigh waves remains in most cases the same, even though the later waves arriving at the stations are of less strength. Station 30 of section BB' might be the exception in this observation, where waves with different frequencies arrive at different times, probably because this station is in the intersection of two regions with deep and shallow soil deposits. Another interesting observation is that Rayleigh waves continue arriving for a longer time at cross section BB' at stations located to the east of station 31, when compared to the rest of the stations. We observe the longest time at station 36. We explain this difference in duration

to the propagation of Rayleigh waves on the eastern part of section BB'. Even though the thickness of the soft deposits in this region (layers 2 and 4) is not sufficiently large (due to the presence of the stiffer layer 7) to induce amplification of the Rayleigh waves, its structure is more similar to a horizontally layered medium where Rayleigh waves can propagate.

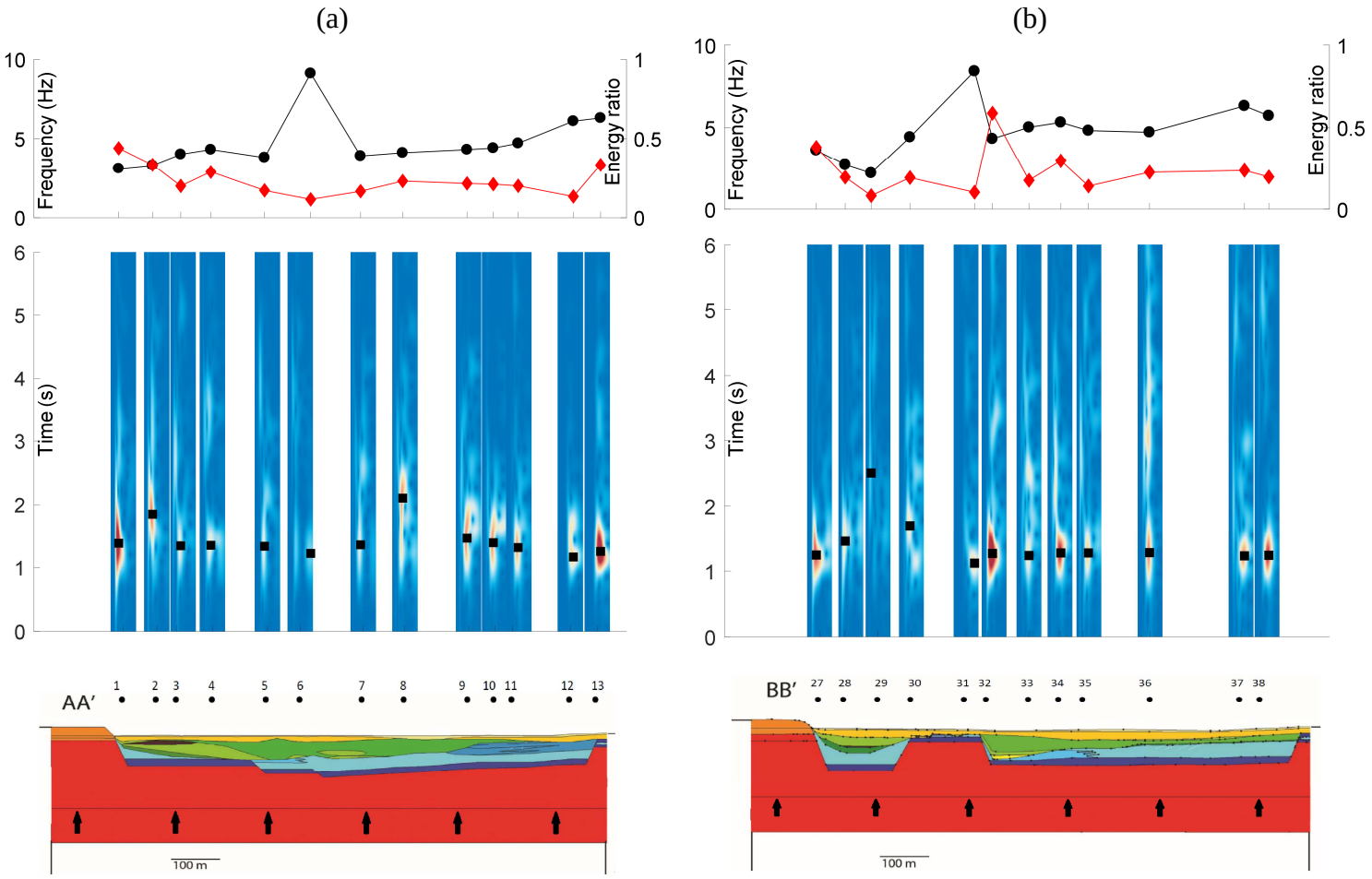

Figure 10. Stockwell transforms of vertical components of extracted Rayleigh waves at stations on cross sections AA' and BB'. (a) Stations on profile AA', (b) Stations on profile BB'. The black squares indicate the times of maximum energy (maximum amplitude of Stockwell Transforms), and the black circles the corresponding frequencies. The red diamonds indicate the total energy ratio at each station.

5. Conclusions

We have applied the Finite Element Method to simulate wave propagation in the Fosso di Vallerano Valley in Rome. We constructed realistic 2D numerical models for the valley from a complex geological model developed in previous studies from geotechnical and geophysical investigations. Using the Normalized Inner Product, we constructed filters for the simulated waveforms at different stations on the surface of the valley, to identify and extract Rayleigh waves. With the isolation of the Rayleigh phases we quantified the amount of surface wave energy present in the seismograms and the corresponding dominant frequencies. Our results illustrate the significant role of the basin edges and soft sediments to concentrate surface wave energy resulting in high amplitudes or longer duration. We found that the strongest Rayleigh waves are generated at the basin edges and that amplification is strongly related to the thickness

of the soil deposits. On the other hand, the elongated duration seems to be more related to a basin structure close to an extended horizontally layered medium where Rayleigh waves are trapped and can propagate. These findings imply that the information due to the high-resolution 2D model was necessary to predict reliable ground motion in the Fosso di Vallerano Valley. In basins located in urban areas, such as the Fosso di Vallerano Valley, where the metropolitan expansion will continue, realistic studies of expected ground motion on a heterogenous structure are required. Finite Element simulations along with the NIP time frequency technique are effective tools to study basin effects such as energy focusing due to a complex basin structure.

A more general perspective to explore in future research may be to quantify the potential of a given basin (geometry, layering,etc.) to generate a large amount of surface waves and consequently to increase the ground motion amplitude and duration. This perspective would be of interest to anticipate aggravation factors for highly heterogeneous basin structures (either 2D or 3D) [34] and to assess the seismic response of long period structures particularly sensitive to surface wave excitation. Furthermore, as proposed by several authors [35,36], future research should also take into account the different uncertainties related to the generation of surface waves, allowing a probabilistic assessment of surface wave phenomena in highly heterogeneous basins.

ACNOWLEDGEMENTS

This research work has been partially financed by internal funding of the BRGM Risk and Prevention Division. We are grateful to an anonymous reviewer for providing valuable suggestions that improved our manuscript.

REFERENCES

[1] Campillo M, Gariel g. C, Nzi K, Sanchez-Sesma FJ. Destructive Strong Ground Motion in Mexico City: Source, Path, and Site Effects during Great 1985 Michoacan Earthquake. Bull Seismol Soc Americ 1989;79:1718–35. doi:http://dx.doi.org/10.1016/0008-8846(77)90075-8.

[2] Abraham J, Lai C, Papageorgiou AS. Basin-effects observed during the 2012 Emilia earthquake sequence in Northern Italy. Soil Dyn Earthq Eng 2015;78:230–42. doi:10.1016/j.soildyn.2015.08.007.

[3] Kawase H, Keiti A. A study on the response of a soft basin for incident S, P, and Rayleigh waves with special reference to the long duration observed in mexico city. Bull Seismol Soc Am 1989;79:1361–82.

[4] Hatayama K, Matsunami K, Iwata T, Irikura K. Basin-Induced Love Waves in the Eastern Part of the Osaka Basin. J Phys Earth 1995;43:131–55.

[5] Boore DM. Basin Waves on a Seafloor Recording of the 1990 Upland, California, Earthquake: Implications for Ground Motions from a Larger Earthquake. Bull Seismol Soc Am 1999;89:317–24.

[6] Liu H-L, Heaton T. Array analysis of the ground velocities and accelerations from the 1971 San Fernando, California, earthquake. Bull Seismol Soc Am 1984;74:1951–68.

[7] Furumura M, Sasatani T, Furumura T. Generation of Basin-Induced Surface Waves Observed in the Tokachi Basin, Hokkaido, Japan. J P 1997;45:287–305.

[8] Olsen KB. Site Amplification in the Los Angeles Basin from Three-Dimensional Modeling of Ground Motion. Bull Seismol Soc Am 2000;90:S77–94.

[9] Kato K, Aki K, Teng T. 3-d simulations of surface wave propagation in the Kanto sedimentary basin, Japan--Part 1: Application of the surface wave gaussian beam method. Bull Seismol Soc Am 1993;83:1676–99.

[10] Maufroy E, Chaljub E, Theodoulidis NP, Roumelioti Z, Hollender F, Bard PY, et al. Source-related variability of site response in the Mygdonian basin (Greece) from accelerometric recordings and 3D numerical simulations. Bull Seismol Soc Am 2017;107:787–808. doi:10.1785/0120160107.

[11] Borcherdt R. Effects of Local Geology on Ground Motion Near San Francisco Bay. Bull Seismol Soc Am 1970;60:29–61.

[12] Lermo J, Chávez-García FJ. Site effect evaluation using spectral ratios with only one station. Bull Seismol Soc Am 1993;83:1574–94. doi:10.1002/bate.200690188.

[13] Beauval C, Bard PY, Moczo P, Kristek J. Quantification of frequency-dependent lengthening of seismic ground-motion duration to local geology: Applications to the Volvi area (Greece). Bull Seismol Soc Am 2003;93:371–85. doi:10.1785/0120010255.

[14] Meza-Fajardo KC, Papageorgiou AS, Semblat J-F. Identification and extraction of surface waves from three-component seismograms based on the normalized inner product. Bull Seismol Soc Am 2015;105. doi:10.1785/0120140012.

[15] Meza-Fajardo KC, Papageorgiou AS. Estimation of rocking and torsion associated with surface waves extracted from recorded motions. Soil Dyn Earthq Eng 2016;80. doi:10.1016/j.soildyn.2015.10.017.

[16] Stockwell RG, Mansinha L, Lowe RP. Localization of the Complex Spectrum: The S Transform. IEEE Trans Signal Process 1996;44:998–1001. doi:10.1109/78.492555.

[17] Humbert P, Fezans G, Dubouchet A, Remaund D. CESAR-LCPC: A computing software package dedicated to civil engineering uses. Bullettin Lab Des Ponts Chaussée 2005;256/257:7–37.

[18] Varone C, Lenti L, Martino S, Semblat JF. Computational assessment of the spatial variability of the seismic ground motion in a recent and highly heterogeneous site-city configuration. Submitted. Geophys J Int n.d.

[19] Ventriglia U. GEOLOGIA DEL TERRITORIO DEL COMUNE DI ROMA. A cura dell'Amministrazione Provinciale di Roma. ROMA: 2002.

[20] Ascani F, Bozzano F, Buccellato A, Monte M Del, Matteucci R, Vergari F. Evoluzione Del Paesaggio E Antiche Vie Di Drenaggio Nell ' Area De " Il Castellaccio " (Roma) Da Indagini Geologiche, Geomorfologiche e Archeologiche. Geol Rom 2008;41:93–116.

[21] Carminati E, Corda L, Mariotti G, Brandano M. Tectonic control on the architecture of a Miocene carbonate ramp in the Central Apennines (Italy): Insights from facies and backstripping analyses. Sediment Geol 2007;198:233–53. doi:10.1016/j.sedgeo.2006.12.005.

[22] Marra F, Florindo F, Boschi E. History of Glacial terminations from the Tiber River, Rome: Insights into Glacial forcing mechanisms. Paleoceanography 2008;23:1–17. doi:10.1029/2007PA001543.

[23] Sottili G, Palladino DM, Marra F, Jicha B, Karner DB, Renne P. Geochronology of the most recent activity in the Sabatini Volcanic District, Roman Province, central Italy. J Volcanol Geotherm Res 2010;196:20–30. doi:10.1016/j.jvolgeores.2010.07.003.

[24] Marra F, Rosa C. Stratigrafia ed assetto geologico dell'area romana. La Geol. di Roma. Cent. Stor., 1995, p. 48–118.

[25] Bozzano F, Lenti L, Marra F, Martino S, Paciello A, Mugnozza GS, et al. Seismic response of the geologically complex alluvial valley at the "europarco business park" (rome - italy) through instrumental records and numerical modelling. Ital J Eng Geol Environ 2016;16:37–55. doi:10.4408/IJEGE.2016-01.O-04.

[26] Bozzano F, Andreucci A, Gaeta M, Salucci R. A geological model of the of the buried Tiber River valley beneath the historical centre of Rome. Bull Eng Geol Environ 2000:1–21.

[27] Marra F, Florindo F. The subsurface geology of Rome: Sedimentary processes, sea-level changes and astronomical forcing. Earth-Science Rev 2014;136:1–20. doi:10.1016/j.earscirev.2014.05.001.

[28] Karner DB, Marra F, Renne PR. The history of the Monti Sabatini and Alban Hills volcanoes: Ground for assessing volcanic-tectonic hazards for Rome. J Volcanol Geotherm Res 2001;107:185–219. doi:10.1016/S0377-0273(00)00258-4.

[29] Karner DB, Marra F. Correlation of fluvio deltaic aggradational sections with glacial climate history: a revision of the classical Pleistocene stratigraphy of Rome. Geol Soc Am Bull 1998;110:748–58.

[30] Marra F, Bozzano F, Cinti FR. Chronostratigraphic and lithologic features of the Tiber River sediments (Rome, Italy): Implications on the post-glacial sea-level rise and Holocene climate. Glob Planet Change 2013;107:157–76. doi:10.1016/j.gloplacha.2013.05.002.

[31] Bozzano F, Buccellato A, Coletti F, Martino S, Marra F, Rivellino S, et al. Analysis of the seismic site effects along the ancient via Laurentina (Rome). Ann Geophys 2017;60. doi:10.4401/ag-7140.

[32] Hughes T.J.R. Linear static and dynamic finite element analysis. Englewood Cliffs, New Jersey: Prentice-Hall; 1987.

[33] Semblat JF, Lenti L, Gandomzadeh A. Asimple multi-directional absorbing layer method to simulate elasticwave propagation in unbounded domains. Int J Numer Methods Eng 2011;85:1543–63. doi:10.1002/nme.

[34] Meza-Fajardo KC, Semblat J-F, Chaillat S, Lenti L. Seismic-wave amplification in 3D alluvial basins: 3D/1D amplification ratios from fast multipole BEM simulations. Bull Seismol Soc Am 2016;106. doi:10.1785/0120150159.

[35] Manolis GD. Stochastic soil dynamics. Soil Dyn Earthq Eng 2002;22:3–15.

[36] Lopez-Caballero F, Modaressi Farahmand Razavi A. Assessment of variability and uncertainties effects on the seismic response of a liquefiable soil profile. Soil Dyn Earthq Eng 2010;30:600–13. doi:10.1016/j.soildyn.2010.02.002.